Nuclear Engineering and Design 360 (2020) 110523

Contents lists available at ScienceDirect

Nuclear Engineering and Design

journal homepage: www.elsevier.com/locate/nucengdes

Numerical investigation on vibration-induced two-phase distribution in a vertical annular channel

Xiu Xiao[a], Yu Guo[a], Minyi Xu[a], Yulong Ji[a], Qingzi Zhu[b,c,*], Mamoru Ishii[c]

[a] Marine Engineering College, Dalian Maritime University, Dalian, Liaoning 116026, China
[b] Department of Mechanical Engineering, Massachusetts Institute of Technology, Cambridge, MA 02139, USA
[c] Department of Nuclear Engineering, Purdue University, West Lafayette, IN 47907, USA

ARTICLE INFO

Keywords:
Two-phase distribution
Horizontal vibration
Bubbly flow
Numerical simulation
Annular channel

ABSTRACT

Earthquake vibrations have great impacts on two-phase flow in the reactor core. In this paper, numerical simulations were conducted to identify the air-water two-phase distribution in a vertical upward annular channel under horizontal vibration condition. The inner and outer diameter of the annular channel are 19.1 mm and 38.1 mm. The simulations were performed based on the two-fluid Euler-Euler modeling framework. Benchmark simulations for bubbly flow under stationary condition were firstly conducted to validate the up-to-date interfacial force models. Applicability of the interfacial force models were evaluated and a set of Ishii-Zuber drag force model, Tomiyama lift force model, Frank wall lubrication force model and Burns turbulent dispersion force model was found to provide the best agreement with experimental results. Based on this work, two-phase flow distributions under vibration condition were studied. Horizontal vibration of the annular channel was simulated by introducing simple harmonic motion. The vibration frequency and vibration amplitude were set to 1.97 Hz and 9.5 mm, respectively. Additional interfacial force caused by inertial effect was imposed on disperse bubbles under vibration condition, which promoted the lateral migration of bubbles. The numerical results showed that the distributions of local interfacial parameters varied periodically along the vibration direction. A maximum increase of about 32% was observed in the peak void fraction compared to that under stationary condition for case 3. But the distribution of local flow parameters remained unchanged in the direction perpendicular to the vibration. A good consistency between the simulation results and the experimental data was found. The comparison results indicate that the present modeling method is able to predict the two-phase distribution of bubbly flow under vibration condition. But an inhomogeneous model considering bubble interactions and grouping is suggested for two-phase flow beyond bubbly regime.

1. Introduction

Two-phase flow is an important phenomenon in nuclear reactor system. With the development of measuring techniques such as impedance meter and probe sensor, a great number of two-phase flow experiments have been conducted to understand the flow behaviors in various kinds of pipes (Kataoka et al., 1985; Hibiki and Ishii, 1999; Lucas et al., 2005; Yang et al., 2013; Tian et al., 2014; Shen et al., 2017). Most of the experiments were performed under stationary condition. But in the past few decades, earthquakes have caused several events on nuclear reactors and its effects on thermal hydraulics and reactor safety have brought public's attention. Researchers have done some fundamental experiments to clarify the vibration effects on two-phase flow. Skoczylas and Urbanski (1992) investigated the influence of vibrating element on heat transfer in a thin layer evaporator experimentally. An increase inheat transfer coefficient value between 23.7% and 104.8% was observed in the investigated range of frequency and amplitude of vibrations. Hibiki and Ishii (1998) studied the local parameters distribution of two-phase flow in a circular pipe with flow-induced vibration. The void fraction profiles changed from wall-peak to core peak or transition at relatively low liquid flow conditions. Mizuno et al. (2014) conducted some experiments on air–water two-phase flow under earthquake acceleration and they observed periodical bubble deformation and trajectory by image processing method. Recently, Xiao et al. (2017) and Chen et al. (2017) conducted some adiabatic air–water two-phase flow experiments under structure vibration conditions using conductivity probe and impedance meter, respectively. Xiao et al. (2017) found that the local interfacial parameters as well as the flow distribution patterns varied continuously with the vibration of test section, and Chen et al. (2017) suggested that the area-averaged void

* Corresponding author at: Department of Mechanical Engineering, Massachusetts Institute of Technology, 77 Massachusetts Avenue, Cambridge, MA 02139, USA.
E-mail address: zhuq@mit.edu (Q. Zhu).

https://doi.org/10.1016/j.nucengdes.2020.110523
Received 9 August 2019; Received in revised form 7 January 2020; Accepted 8 January 2020
0029-5493/

Nomenclature

$\vec{a}$	vibration acceleration (m/s^2)
C	coefficient
d	diameter (m)
D	pipe diameter (m)
E	vibration amplitude (mm)
Eo	Eötvös number
Eo'	modified Eötvös number
f	vibration frequency (Hz)
$\vec{F}$	Interfacial force (N)
$\vec{g}$	gravity acceleration (m/s^2)
j	superficial velocity (m/s)
k	turbulent kinetic energy (m^2/s^2)
K	interfacial momentum exchange coefficient
m	power law coefficient
p	pressure (Pa)
r	radial distance from the centerline of the annulus (m)
R_i	inner diameter of the annular channel (m)
R_o	outer diameter of the annular channel (m)
Re	Reynolds number
S	vibration displacement (mm)
Sr	shear rate
Sc	Schmidt number
t	time (s)
$\vec{v}$	velocity vector (m/s)
v_T	terminal velocity (m/s)
y_w	distance to the nearest wall (m)
z	measurement location under stationary condition (m)
z'	measurement location under vibration condition (m)

Greek symbols

α	void fraction
ρ	density (kg/m^3)
μ	viscosity (m^2/s)
θ	vibration angle (rad)
ω	vibration angular velocity (rad/s)
σ	surface tension coefficient (N/m)
Γ	vibration phase

Superscripts and Subscripts

b	bubble
h	equivalent hydraulic diameter (m)
k	phase symbol
g	gas phase
l	liquid phase
m	maximum value
w	wall
wd	damping coefficient
wc	cut-off coefficient
D	drag force
L	lift force
W	wall lubrication force
TD	turbulent dispersion force
IN	inertial effect induced interfacial force
t	turbulent fluctuation

Operators

$< >$	area-averaged quantity

fraction may decrease under structure vibration due to the increase of distribution parameter in bubbly flow. Unfortunately, the comprehensive two-phase flow information cannot be

captured regardless of the measuring instruments adopted in these experiments. Further investigations on vibration effects were suggested in both studies.

In recent years, Computational Fluid Dynamics (CFD) has become a very useful tool for two-phase flow analysis and prediction since it can provide detailed information which might be difficult to obtain through experiments. Currently, two-fluid model is the most popular and extended formulation for gas–liquid flow systems. In the two-fluid model, gas and liquid phases are treated separately in terms of two sets of conservation equations (Ishii and Hibiki, 2010). The interfacial transfer term that appears in the balance equations is one of the most important characteristics of two-fluid model. Closure equations are required to describe the interaction terms between two phases and they can determine the predictive capability of two-fluid model to a large extent. The interfacial forces in the momentum equation are generally considered to include drag force, lift force, wall lubrication force, virtual mass force and turbulent dispersion force, as illustrated in Fig. 1 (Wang and Yao, 2016). A complete description of these forces determines the phase distribution pattern across the transverse section of the channel in bubbly flow. A series of calculation formula have been proposed for each force by different researchers, and some work have been done to evaluate the force models (Lucas et al., 2004; Rzehak et al., 2012; Yamoah et al., 2015; Chuang and Hibiki, 2017). But confusion still exists in selection of the force models because of the absence of full insight into the predictive features of different models. Therefore, to obtain reliable calculation results, it is necessary to test the validation of each model for specific flow condition before using it. With regard to earthquake condition, the vibration of the test section could further change the effective interfacial forces acting on bubbles, leading to continuous variations in flow distributions. Thus, it is necessary to determine the predictive capability of CFD method for calculating the transient two-phase flow distributions under vibration conditions.

This paper is a part of the ongoing study on adiabatic air–water two-phase flow under earthquake condition. The test section is a vertical upward annular channel with a total height of 2.32 m. The inner and outer diameter of the annular channel are 19.1 mm and 38.1 mm, respectively. In this study, simulations on bubbly flow under stationary condition are firstly conducted. The performances of each interfacial force model are comparatively analyzed and a set of interfacial force models applicable for bubbly flow in the vertical annular channel is proposed. Based on this work, numerical simulations on bubbly flow under horizontal vibration condition are conducted by introducing simple harmonic motion to the flow channel. The vibration frequency and amplitude are set to 1.97 Hz and 9.5 mm. The transient two-phase flow phenomena under vibration condition are calculated, and the

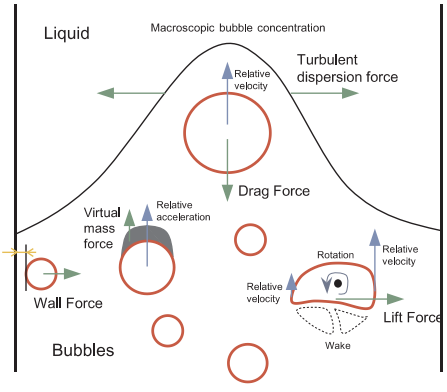

Fig. 1. Interfacial forces in bubbly flow (Wang and Yao, 2016).

comparison results with the experimental data suggest that the present modeling method provides a promising way for predicting the two-phase distribution of bubbly flow under vibration condition.

2. Model description

2.1. Field equations

The simulation is based on Euler-Euler two-fluid model framework. In bubbly flow with relatively low void fraction, bubble density is small and bubble interactions are quite rare. Therefore, bubble coalescence and breakup are not taken into account in the present model. Reasonability of this simplification has been confirmed by experimental results (Xiao et al., 2017). Based on this assumption, the mono-dispersed model in which the bubbles are equally sized is adopted. The bubble diameter D_b is only related to the inlet flow condition and it keeps constant during flow process. Denoting the liquid phase as continuum ($k = l$) and the gas bubbles as disperse phase ($k = g$). For adiabatic air–water two-phase flow, mass and heat transfer between phases do not exist. Therefore, the conservation equations for gas–liquid two-phase flow under stationary condition can be written as follows:

Continuity equation:

$$\frac{\partial(\alpha_k\rho_k)}{\partial t} + \nabla\cdot(\alpha_k\rho_k\vec{v_k}) = 0$$

Momentum equation:

$$\frac{\partial(\alpha_k\rho_k\vec{v_k})}{\partial t} + \nabla\cdot(\alpha_k\rho_k\vec{v_k}\vec{v_k}) = -\alpha_k\nabla p + \alpha_k\rho_k\vec{g} + \nabla\cdot[\alpha_k\mu_k(\nabla\vec{v_k} + \vec{v_k}^T)] + \vec{F_k}$$

In the above equations, α_k, ρ_k, $\vec{v_k}$ and μ_k are the local void fraction, the density, the velocity and the effective viscosity of phase k respectively. p stands for the pressure and $\vec{g}$ is the gravity acceleration. $\vec{F_k}$ is the total interfacial force.

Apart from the interfacial forces, turbulent viscosity also needs to be solved by closure equations. Unfortunately, standard turbulence model applicable to all types of flow has not been proposed yet. But it has been proved that the Shear Stress Transport (SST) model developed by Menter (1994) can provide more realistic prediction for two-phase flow compared to the other turbulence models (Yamoah et al., 2015). The SST model can be seen as a combination of the standard k-ε model (Launder and Spalding, 1974) and k-ω model (Wilcox, 1998). Through applying the two-equation k-ε model in the bulk flow and the two-equation k-ω model near the wall, the SST model improves the robustness and accuracy of turbulence calculation greatly. Thus, turbulence of the liquid phase is calculated by SST model in this work. The concrete introduction of this model can be found in reference (Menter, 1994). Furthermore, the turbulence of dispersed bubbly flow is calculated using a zero equation turbulence model and the bubble-induced turbulence has been taken into account according to Sato's model (Sato and Sekoguchi, 1975).

2.2. Interfacial forces

The total interfacial force $\vec{F_k}$ in the momentum equation includes drag force, lift force, wall lubrication force, virtual mass force and turbulent dispersion force, as illustrated in Fig. 1. Frank et al. (2008) pointed out that the virtual mass force is of minor importance compared with the other drag and non-drag forces and can be neglected. Thus, the total interfacial force has the following expression:

$$\vec{F_k} = \vec{F_D} + \vec{F_L} + \vec{F_W} + \vec{F_{TD}}$$

Here, the subscripts D, L, W and TD represent the drag force, lift force, wall lubrication force and turbulent dispersion force, respectively. As mentioned above, various empirical expression for each interfacial force have been proposed, but these force models are still subject to considerable difference. This is because each model was proposed under some specific assumptions and was only fitted in the experiments performed under limited flow conditions. Table 1 summarizes the up-to-date available interfacial force models. The comprehensive introduction of these models which can be found in related references will not be repeated here. For bubbly flow in the vertical upward annular channel, the appropriate interfacial force models need to be confirmed by the corresponding experimental results before applying them to vibration condition. The detailed model assessment will be discussed in Section 4.

When the vertical annular channel was driven by an eccentric cam

Table 1
Interfacial force models.

Interfacial forces	Force models	Model correlations
Drag force	Schiller and Naumann (1935)	$C_D = \begin{cases} 24(1 + 0.15\mathrm{Re}_b^{0.687})/\mathrm{Re}_b & \mathrm{Re}\leqslant 1000 \\ 0.44 & \mathrm{Re} > 1000 \end{cases}$
	Grace et al. (1976)	$C_D = \max(\min(C_{D,ellipse}, C_{D,cap}), C_{D,sphere})C_{D,ellipse} = \frac{4}{3}\frac{gd_b}{v_T^2}\frac{(\rho_l-\rho_g)}{\rho_l}$, $C_{D,cap} = \frac{8}{3}$, $C_{D,sphere} = \begin{cases} 24(1 + 0.15\mathrm{Re}_b^{0.687})/\mathrm{Re}_b & \mathrm{Re}_b\leqslant 1000 \\ 24/\mathrm{Re}_b & \mathrm{Re}_b > 1000 \end{cases}$
	Ishii and Zuber (1979)	$C_D = \max(\min(C_{D,ellipse}, C_{D,cap}), C_{D,sphere})C_{D,ellipse} = \frac{2}{3}Eo^{1/2}$, $C_{D,cap} = \frac{8}{3}$, $C_{D,sphere} = \max\left(\frac{24}{\mathrm{Re}_b}(1 + 0.15\mathrm{Re}_b^{0.687}), 0.44\right)$
Lift force	Legendre and Magnaudet (1998)	$C_L = \sqrt{(C_{L,low\,\mathrm{Re}})^2 + (C_{L,high\,\mathrm{Re}})^2}C_{L.low\,\mathrm{Re}} = \frac{6}{\pi^2}(\mathrm{Re}_b\,Sr)^{-0.5}\frac{2.55}{(1+0.2\,\mathrm{Re}_b/Sr)^{1.5}}$, $C_{L.high\,\mathrm{Re}} = \frac{1}{2}\frac{1+16\,\mathrm{Re}_b^{-1}}{1+29\,\mathrm{Re}_b^{-1}}$
	Tomiyama (1998)	$C_L = \begin{cases} \min[0.28\tanh(0.12\mathrm{Re}_b), f(Eo')] & Eo' \leqslant 4 \\ f(Eo') & 4 < Eo' \leqslant 10 \\ -0.27 & 10 < Eo' \end{cases}$ $\mathrm{f}(Eo') = 0.00105Eo'^3 - 0.0159Eo'^2 - 0.0204Eo' + 0.474$
Wall force	Antal et al. (1991)	$C_W = \max\left(0, \frac{C_{w1}}{d_b} + \frac{C_{W2}}{y_w}\right)C_{w1} = -0.01$, $C_{W2} = 0.05$or$C_{w1} = -0.064$, $C_{W2} = 0.016$
	Tomiyama (1998)	$C_W = C_{WL}\frac{d_b}{2}\left(\frac{1}{y_w^2} - \frac{1}{(D-y_w)^2}\right)C_{WL} = \begin{cases} 0.47 & Eo < 1 \\ e^{-0.933Eo+0.179} & 1 < Eo \leqslant 5 \\ 0.00599Eo - 0.0187 & 5 < Eo \leqslant 33 \\ 0.179 & 33 < Eo \end{cases}$
	Frank et al. (2008)	$C_W = C_{WL}\max\left(0, \frac{1}{C_{wd}}\cdot\frac{1-y_w/(C_{wc}d_b)}{y_w(y_w/(C_{wc}d_b))^{m-1}}\right)C_{wd} = 6.8$, $C_{wc} = 10.0$, $m = 1.7$or$m = 1.0$
Turbulent dispersion force	Lopez de Bertodana (1992)	$\vec{F_{TD}} = -C_{TD}\rho_l k_l\nabla\alpha_g$, $C_{TD} = 1$
	Burns et al. (2004)	$\vec{F_{TD}} = -C_{TD}C_D\frac{\mu_l^t}{Sc}\left(\frac{\nabla\alpha_g}{\alpha_g} - \frac{\nabla\alpha_l}{\alpha_l}\right)$, $C_{TD} = 1$, $Sc = 0.9$

fixed on top of the test section, it started to vibrate periodically with specific frequency and amplitude. The vibration system is shown in Fig. 2 (Xiao et al., 2017). For the dispersed bubbles in the vibrating channel, additional interfacial force is imposed on bubbles due to inertial effect. This force has the following expression:

$$\overrightarrow{F_{IN}} = -(\alpha_g \rho_g + \alpha_l \rho_l)\overrightarrow{a}$$

Here, $\overrightarrow{a}$ represents the vibration acceleration, which directly determines the scale of additional interfacial force. Thus, the transient total interfacial force becomes

$$\overrightarrow{F_k} = \overrightarrow{F_D} + \overrightarrow{F_L} + \overrightarrow{F_W} + \overrightarrow{F_{TD}} + \overrightarrow{F_{IN}}$$

As a result, the bubble forces in radial direction is unbalanced and lateral bubble migration takes place once the annular channel starts to vibrate, leading to redistribution of two-phase flow patterns.

3. Numerical details

The numerical simulations were conducted on the platform of ANSYS CFX (v18.0). For model validation purpose, the geometry structure of the two-phase flow channel in the simulation calculations was the same as that in the experiment reported in an earlier literature (Xiao et al., 2017). The test section was a vertical upward annular channel with a total height of 2.32 m. The inner and outer diameters of the annular channel were 19.1 mm and 38.1 mm, respectively. During the experiment, the local interfacial parameters including the void fraction, the interfacial area concentration and the Sauter mean diameter of bubbles were measured by four-sensor conductivity probe. The measurement location was $z/D_h = 77$, where z was the axial position along the annular channel and D_h was the equivalent hydraulic diameter of the annulus. To confirm the validity of the modeling method, the two-phase flow parameters at the corresponding axial location calculated by the simulation were compared with those measured by the conductivity probe.

A total of four cases within bubbly flow regime were selected in the numerical simulations. All the flow cases were set according to the experimental conditions (Xiao et al., 2017). Table 2 shows the detailed flow parameters of these simulation cases. For each case, a fixed bubble diameter was given based on the average Sauter mean diameter measured by the conductivity probe in the corresponding experiment. Based on the grid dependence analysis provided in Section 4.1, benchmark simulations for bubbly flow under stationary condition were performed

Table 2
Flow parameters of the four cases used in the simulations.

Parameters	Unit	Case 1	Case 2	Case 3	Case 4
Liquid density, ρ_l	kg/m^3	997.8			
Liquid viscosity, μ_l	kg/m·s	8.9×10^{-4}			
Gas density, ρ_g	kg/m^3	1.185			
Gas viscosity, μ_g	kg/m·s	1.83×10^{-5}			
Surface tension, σ	N/m	0.072			
Superficial liquid velocity, j_l	m/s	0.256	0.258	0.520	0.521
Superficial gas velocity, j_g	m/s	0.043	0.153	0.101	0.199
Void fraction, α	–	0.08	0.22	0.10	0.19
Bubble diameter, D_b	mm	2.75	6.50	3.25	3.30
Bubble Reynolds number, Re_b	–	877	2653	1536	1270
Eötvös number, Eo	–	1.03	5.73	1.43	1.48

to validate the models of each force. Following this work, simulations on two-phase flow in the vibrating channel were conducted. As with the experiment, the annular channel vibrated horizontally around z axis. The vibration frequency and amplitude were set to 1.97 Hz and 9.5 mm, respectively. It is worth noting that the vibration parameters are set based on the investigation on earthquake information by Chen (2012). During the two-phase flow experiment under vibration condition, the motor speed was set to 120 rpm with the theoretical vibration frequency being 2.0 Hz. However, due to the gravity effect of the structure components and the damping effect of the springs, the vibration of the test section was not an ideal simple harmonic motion. The vibration acceleration of the test section was analyzed by FFT method and it was found that the actual vibration frequency was 1.97 Hz. Therefore, to be consistent with the experimental conditions, the vibration frequency was set to 1.97 Hz in the numerical simulations. Furthermore, for simplification purpose, the damping effect of the springs in the experiment was not considered and the vibration was regarded as a simple harmonic motion having the following expressions.

Vibration angle:

$$\theta = \theta_m sin(2\pi ft) = 0.00415 sin(3.94\pi t)(rad)$$

Angular velocity:

$$\omega = 2\pi f \theta_m cos(2\pi ft) = 0.05 cos(3.94\pi t)(rad/s)$$

Vibration acceleration:

$$a = (2\pi f)^2 z' \theta_m sin(2\pi ft) = 0.62 z' sin(3.94\pi t)(m/s^2)$$

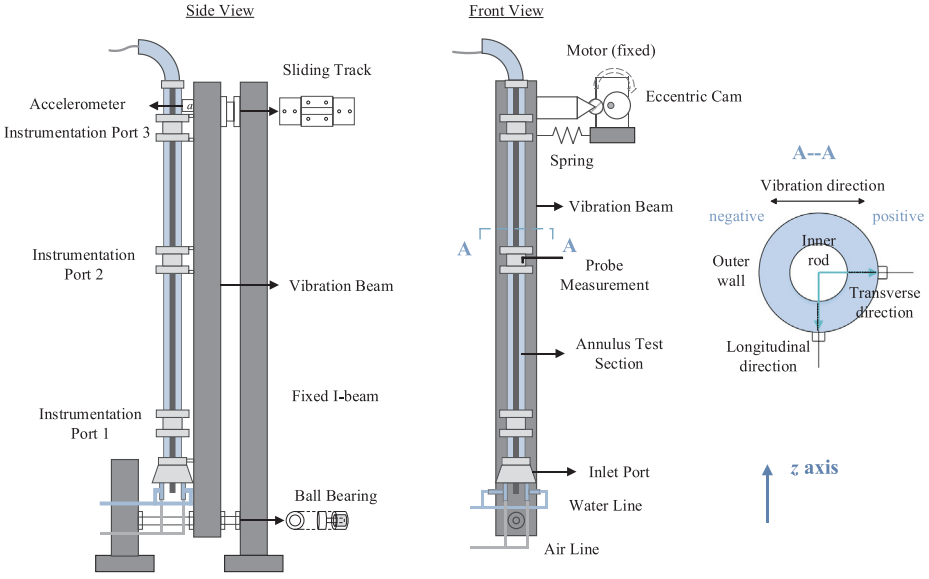

Fig. 2. Schematic diagram of two-phase flow system under vibration condition.

where, θ_m and f represent the maximum vibration angle (rad) and the vibration frequency (Hz) of the annular channel. $z^{'}$ is the axial location of the measurement point along the vibrating annular channel which doesn't vary with the vibration angle. Fig. 3 shows the profiles of the vibration acceleration used in the simulations and experiments, respectively. The comparison result suggests that the simulated motion can approximate the vibration of the test section in the experiment despite of the finite discrepancy.

Uniform distributions of gas and liquid velocities were applied at the inlet of the annular channel. The outlet was set to atmospheric pressure. The wall boundary conditions were set as no-slip condition for the liquid phase and free-slip condition for the gas phase assuming that direct contacts between the walls and the bubbles were negligible. The solver was based on the finite volume method. High resolution was selected as the advection scheme to control numerical diffusive discretization errors and the coupled volume fraction option was used in the simulations (Sharma et al., 2017). For the transient calculation of two-phase flow under vibration condition, the output of the simulation under stationary condition was used as the initial characterization. The time step was set to 0.001 s and the Root Mean Square (RMS) residual target of 1×10^{-4} was taken as the reliable criterion for convergence of the numerical simulation (Yamoah et al., 2015).

4. Results and discussion

4.1. Grid dependence

Grid sensitivity analysis was conducted in this section. An increase of node number in both the annulus cross-section and the channel length was used to reach the mesh independence. The node distribution settings are shown in Table 3. The experimental results of case 1 were used to verify the grid independence. Fig. 4 displays the comparisons of simulation and experimental results. It can be seen from Fig. 4(a) that the phase distribution along the annulus radius is obtained by numerical simulation and good consistency is achieved between the simulation and experimental results. Significantly, the radial distribution of void fraction doesn't show significant variations with the increase of node number. Especially, the numerical simulation results with a node resolution of 840 × 464 are basically the same with that of 1600 × 618. It indicates that the macroscopic two-phase bubbly flow simulation has a relatively low requirement on grid resolution. This statement agrees well with the finding in reference (Wang and Yao, 2016). To reduce computational cost and satisfy mesh independence, a total node number of 389,760 has been chosen for numerical simulation.

In addition, it is known that special attention should be paid when selecting the mesh size adjacent to the wall. Sarı et al. (2009) recommended that a wall distance value (y^+) larger than ~30 can accurately model the wall effects. But the grid sensitivity results in Fig. 4(a) suggests that the variations of two-phase flow parameters near the wall can also be well captured when y^+ less than30. To further study the numerical simulation dependence on y^+ value, three node distribution patterns were considered with a fixed total node number of 389760. The y^+ value varies from 13 to 37. As can be seen from Fig. 4(b), a mesh with fine cells near the wall region (Test 4) doesn't improve the simulation results compared to the even distribution (Test 2), but the coarse grid distribution at the walls (Test 5) can results in a relatively lower gradient of the close-wall phase distribution. To this end, the y^+ value shows a small effect on the two-phase flow pattern near the wall in our flow cases.

4.2. Validation of interfacial force models

The models of interfacial forces were evaluated sequentially by experimental results in this part. To determine the performances of different force models, the simulations need to be performed by changing the models of considered force while keeping the models of the other forces constants. Based on previous experiences, the following set of interfacial force models was chosen as the simulation basis (Yamoah et al., 2015). The Ishii-Zuber model was used for drag force, the Tomiyama model for lift force, the Frank model for wall force and the Burns model for turbulent dispersion force. The predictive features of the concerned force models were analyzed by using the void fraction profiles measured in the corresponding experiment.

The three drag force models which are the Schiller-Naumann model, the Grace model and the Ishii-Zuber model as shown in Table 1 were firstly evaluated for all the four flow cases. Fig. 5 shows the simulation results for case 1 and case 3. It can be clearly seen that the void fraction distributions are well captured by the Grace model and the Ishii-Zuber model. Both of these two models have taken into account the bubble distortion phenomenon and modified the drag coefficient C_D for the ellipsoidal bubble regime. Different from the above two models, the Schiller-Naumann model doesn't consider bubble distortion and uses a common function of drag coefficient. As a result, the void fraction near the wall is underestimated by Schiller-Naumann model. By comparison, it is suggested that the Ishii-Zuber model can best predict the void fraction profile for bubbly flow in the annular channel. This result also applies to case 2 and case 4.

The lift force is essential for predicting the lateral distribution of bubbles since it acts perpendicular to the relative motion of gas and liquid phases. The lift force models tested in this paper includes the Legendre-Magnaudet model and the Tomiyama model. The simulation results of different lift force models for case 1 and case 2 are presented in Fig. 6. For case 1 with relatively low void fraction and bubble Reynolds number Re_b, the Tomiyama model can well predict the radial phase distribution. The simulations on case 3 and case 4 give similar results. But as the gas velocity increases, bubble coalescence occurs and big bubbles are pushed to the pipe center, resulting in the center-peak profile in phase distribution, as shown by black solid squares in Fig. 6(b). For this flow condition, although the Tomiyama model can capture the change of sign in the lift force coefficient, it still overestimates the void fraction near the wall. One possible reason is that bubble interactions cannot be neglected and the size of bubbles plays an important role in determining the flow pattern, which means that mono-dispersed model is not applicable to such condition any more. Fig. 6 also shows that the Legendre-Magnaudet model which provides higher C_L values underestimates the wall effect for all the flow cases, especially for case 2 with relatively high Re_b and Eo. This is because the Legendre-Magnaudet model is only applicable to the two-phase flow conditions with bubble Reynolds number less than 500 and it doesn't take bubble deformation into consideration (Legendre and Magnaudet, 1998). Therefore, the Tomiyama lift force model is suggested for bubbly flow in the vertical annular channel.

Following the optimization of drag force and lift force models, the

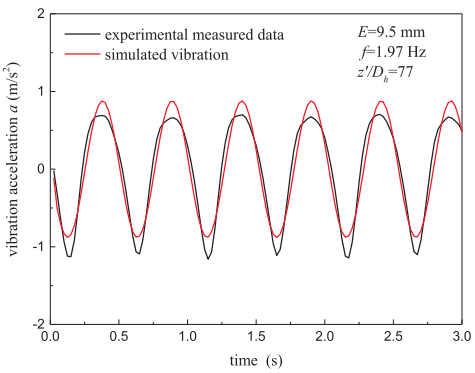

Fig. 3. Comparison of vibration acceleration used in the simulations and experiments.

Table 3
Node distribution settings for grid dependence analysis.

Parameters	Test 1	Test 2	Test 3	Test 4	Test 5
Radial node number	10	15	20	15	15
Number of nodes in cross section	400	840	1600	840	840
Axial node number	310	464	618	464	464
Total node number	124,000	389,760	988,800	389,760	389,760
Node distribution pattern	Even	Even	Even	Gird ratio = 1.2	One coarse grid at both walls
y^+	26	17	14	13	37

comparison of wall force models is performed among the Antal model, the Tomiyama model and the Frank model. The original coefficients of the Frank model (C_{wd} = 6.8, C_{wc} = 10, m = 1.7) is slightly modified and a new set of coefficients (C_{wd} = 6.8, C_{wc} = 10, m = 1.2) has been introduced in this study. Fig. 7 shows the calculation results for case 3 and case 4. Compared with the experimental results, the Antal model underestimates the wall effects for both flow cases, which results in a higher void fraction at the vicinity of the wall and a lower gas distribution in the central region of the annulus . On the contrary, the wall force coefficient C_{WL} calculated by the Tomiyama model is very high and the predicted void fraction in the near wall region is much lower than the experimental results. In general, the Frank model gives satisfactory results for all the considered flow cases.

In two-phase flow, the turbulent dispersion force is correlated with the turbulent parameters, such as turbulent viscosity and turbulent kinetic energy, as depicted in Table 1. Wang and Yao (2016) suggested that the influence of turbulent dispersion model on the simulation results can be neglected at the macroscopic scale if the turbulent model and turbulent viscosity model were fixed. Yamoah et al. (2015) gave similar conclusion from their numerical investigations. Thus, the most used turbulent dispersion force model proposed by Burns with C_{TD} = 1.0 is directly adopted in this work. As can be seen from Figs. 5-7, the Burns model shows fairly good outcome in fitting the simulation results to the experimental measurements given that the other force models are suitably selected, especially for case 1, case 3 and case 4.

4.3. Benchmark simulations

Based on the above validation work, a set of Ishii-Zuber drag force model, Tomiyama lift force model, Frank wall force model and Burns turbulent dispersion force model is suggested to provide the best agreement with the experimental results. In this part, benchmark simulations were conducted for all the four bubbly flow cases under stationary condition. Fig. 8 shows the void fraction and interfacial area concentration profiles obtained from numerical simulations and physical experiments. As expected, the radial distributions of two-phase flow parameters were well predicted by the numerical method for case 1, case 3 and case 4. But larger deviations exist between the calculated results and the measured data for case 2. This is because, under fully developed bubbly flow conditions, the local flow parameters profiles are governed by the balance of lateral interfacial forces acting on bubbles and the applicability of the interfacial force models is dependent on specific flow conditions and bubble regimes. Case 2 lies in the transition regime from bubbly flow to slug flow, where coalescence between disperse bubbles has become an important phenomenon. Bubble deformation and interactions cannot be neglected in such flow condition, resulting in the poly-disperse nature being the main contributor to the flow characteristics. Therefore, the poly-dispersed flow model considering bubble coalescence and breakup is suggested for case 2 in the future work (Frank et al., 2008).

4.4. Phase distributions in the vibrating annular channel

In simulating bubbly flow under vibration condition, the annular channel was set to vibrate periodically following the vibration parameters described in Eqs.(1)-(3). This paper focuses on the validation of the numerical modeling method for bubbly flow under horizontal vibration condition. Case 3 and case 4 were calculated in this part for clarification. In accordance with the axial position of the conductivity probe in the experiment, the simulation outputs at axial location of z/D_h = 77 were analyzed. In processing the experimental data under vibration condition, each vibration cycle was divided into twelve vibration phases and the statistical average values in each phase were used to represent the transient flow parameters at a specific vibration position (Xiao et al., 2017). For comparative analysis, the transient simulation results at the corresponding vibration positions were used to depict the vibration-induced variation of flow distributions in the annular channel.

Fig. 9 shows the variations of void fraction contour during one vibration cycle for case 3. It can be seen that the void fraction experiences a periodical change with the vibration of the annular channel. When the annular channel vibrates from the vertical position towards the maximum displacement position in the negative direction (*i.e.* Γ = 0 to Γ = 4), the liquid phase tends to cluster to the left side of the annulus and the bubbles are pushed to the right side. As a result, the void fraction shows higher values on the left side of the outer wall and inner rod. More specifically, along the radius in the transverse direction as shown in Fig. 2, the void fraction at the radial position of $(r\text{-}R_i)/(R_o\text{-}R_i)$ = 0.8 can reach 0.16 when the channel vibrates to Γ = 4. This value is 24% higher than the corresponding local void fraction under stationary condition. Opposite trend can be found when the annular channel vibrates from the maximum displacement position in the positive direction (*i.e.* Γ = 10) back to the vertical position. The peak void fraction which appears in the left part of the annulus cross section can be up to 0.184, about 32% higher than the peak void fraction under

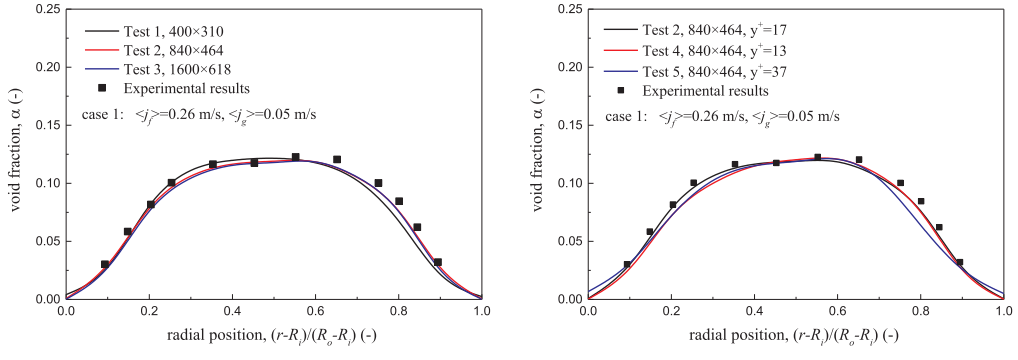

Fig. 4. Simulation results of grid dependence tests.

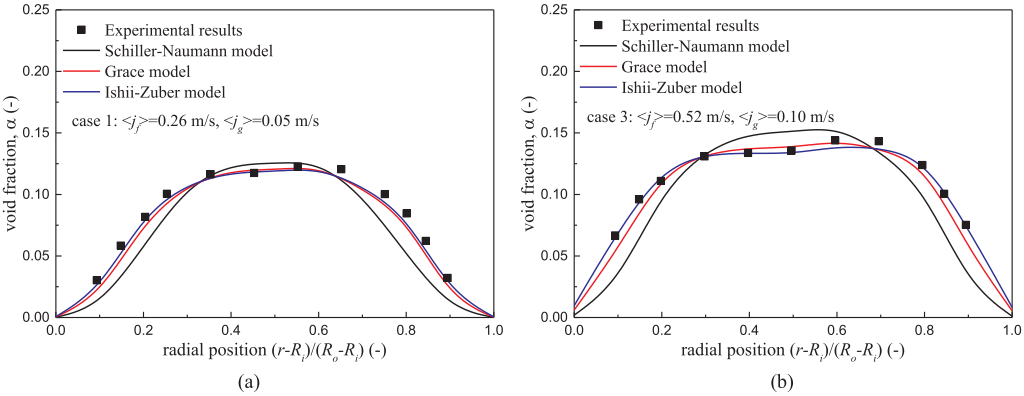

Fig. 5. Simulation results of various drag force models for different flow cases.

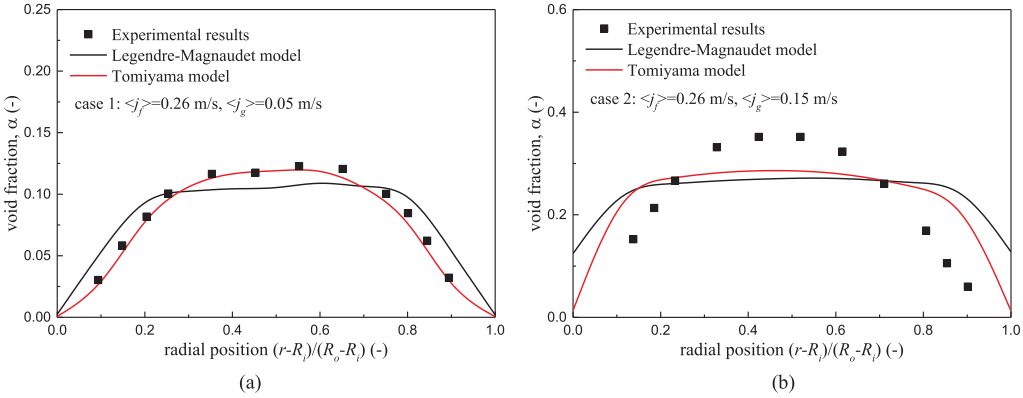

Fig. 6. Simulation results of various lift force models for different flow cases.

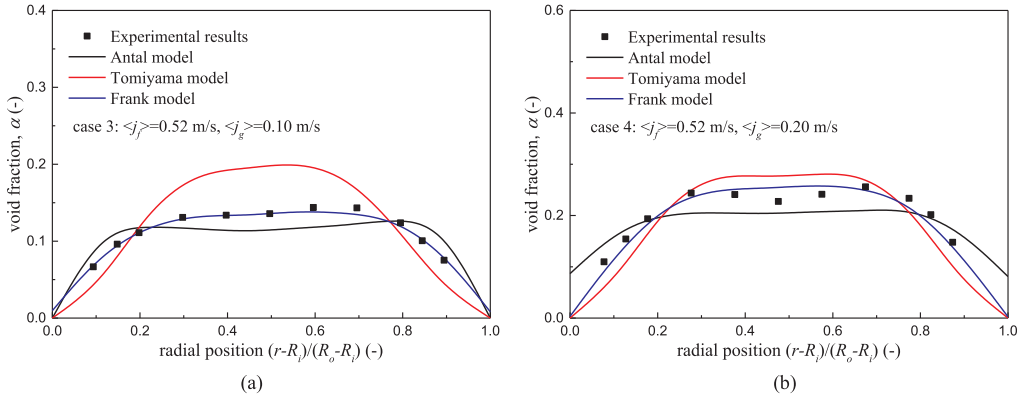

Fig. 7. Simulation results of various wall force models for different flow cases.

stationary condition. Similar phenomena can also be found in the other flow cases, which are consistent with the experimental observations. Such result also indicates that the additional interfacial force caused by the inertial effect plays a great role in determining the two-phase distribution under structure vibration condition.

To further confirm the predictive capability of the numerical modeling method, the local void fraction distributions are compared with the experimental results in some specific vibration phases. The considered radius lies in the transverse direction depicted in Fig. 2. The detailed comparison results are presented in Fig. 10. The solid symbols represent the measured data in the experiments while the solid lines stand for the calculation results in both subfigures. Apparently, for all the flow cases, the simulation method can not only capture the variation characteristics of phase distribution in the vibrating annular channel, but also has very limited deviations. As can be seen from this figure, strong peaks skewed to outer wall are formed in the void fraction profiles as the annular channel vibrates to phase 4. It is worth noting that the peak values obtained in the experiments are 11.2% and 4.2% higher than the simulation results and the radial positions where the peaks are located have some offset. One of the important reasons is the difference between the simplified harmonic motion and the actual vibration of the annular channel. At this vibration phase, the actual vibration acceleration is higher because of the effects of spring damping and the other system structures, as shown in Fig. 3. Therefore, the bubbles are imposed with larger additional interfacial force in the experiment, leading to relatively higher peak values. This difference decreases with the increase of void fraction considering that the inertial effect on the disperse bubble decreases with the void fraction. On the contrary, the void fraction profiles show skewed inner rod peaks at vibration phase 10, which are consistent with the measurement data.

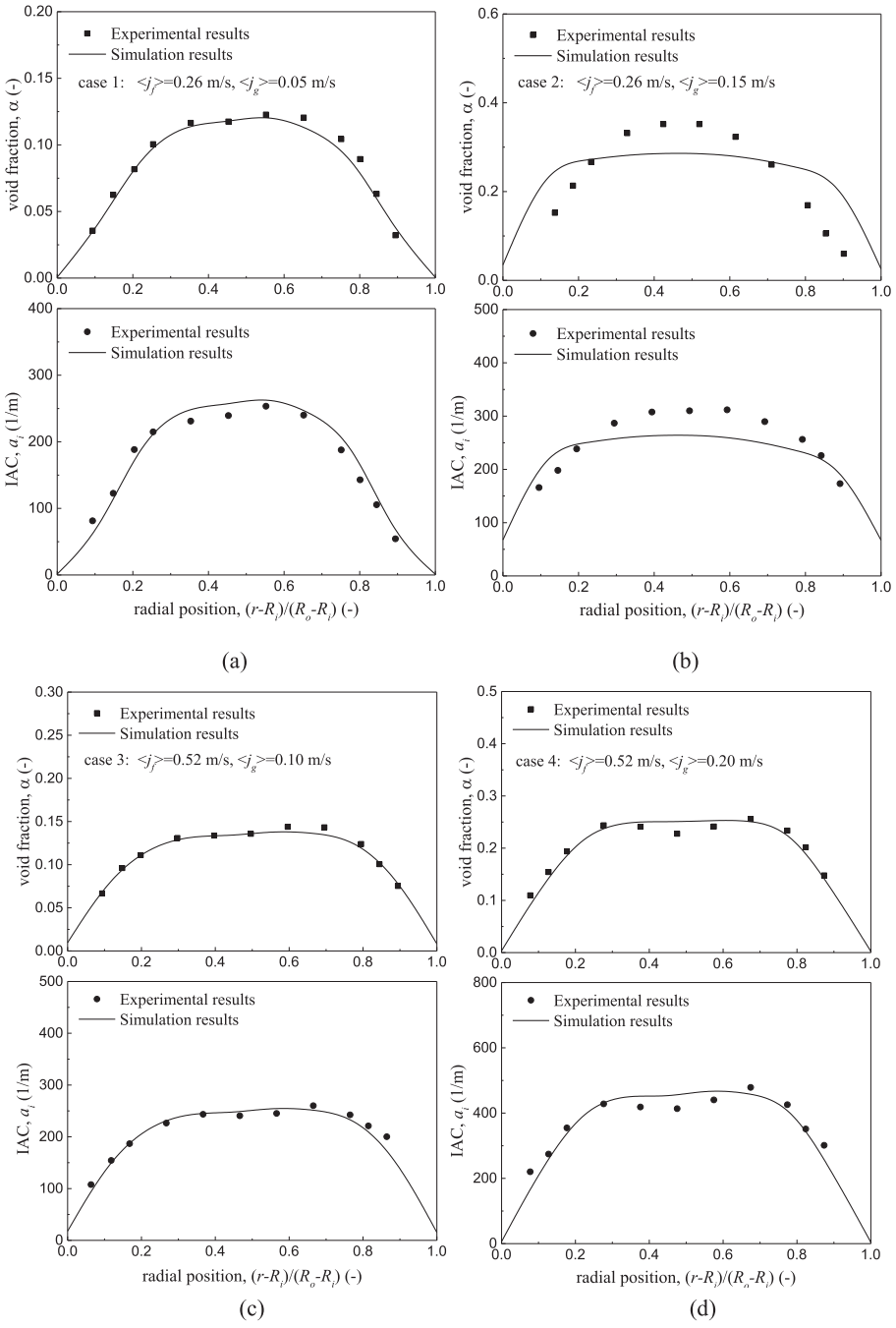

Fig. 8. Simulation results of void fraction and interfacial area concentration profiles.

Finally, the void fraction starts to decrease near the inner rod region and increase near the outer wall region as the flow channel moves to the vertical position (*i.e.* $\Gamma = 12$). It can be observed that there are very good agreements between the simulation results and experimental data at this stage.

Based on the analysis above, the numerical modeling method can be convincingly used to predict the detailed bubble transport phenomena throughout the whole vibration process. The distribution pattern of two-phase bubbly flow in the vertical annular channel is supposed to change constantly with structure vibration. Fig. 11 shows the successive variations of local void fraction and interfacial area concentration profiles in one vibration period. The peak void fraction and the peak IAC as well as their radial locations change continuously. Comparative analysis indicates that the dynamic phase distributions are the same with the experimental observations. This paper focuses on the validation of numerical modeling method for bubbly flow under structure vibration condition. The specific description on bubble migration and flow structure transformation which can be found in an earlier study (Xiao et al., 2017) will not be repeated here.

So far, our study has focused on the vibration-induced bubble transport phenomena along the radius in the transverse direction. In fact, bubble migrations take place throughout the whole cross section of the vibrating annulus. In particular, the phase distribution along the horizontal direction perpendicular to the vibration is discussed in this section. The current concerned radius lies in the longitudinal direction depicted in Fig. 2. Fig. 12 displays the variations of void fraction profile in one vibration period for both cases. Different from the above results, the phase distribution patterns in this direction are not significantly affected by the vibration of the annular channel and the local void fraction basically remain unchanged. The reason for this phenomena is

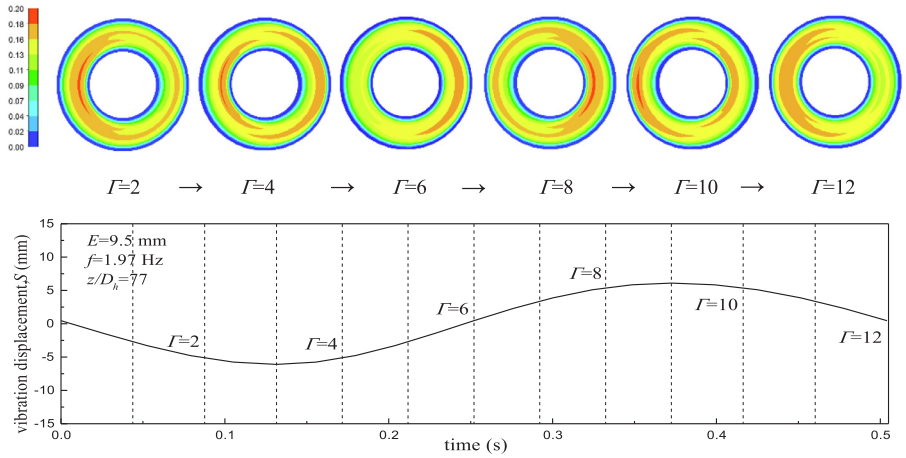

Fig. 9. Variations of two phase distribution in the cross section of the annulus under structure vibration condition.

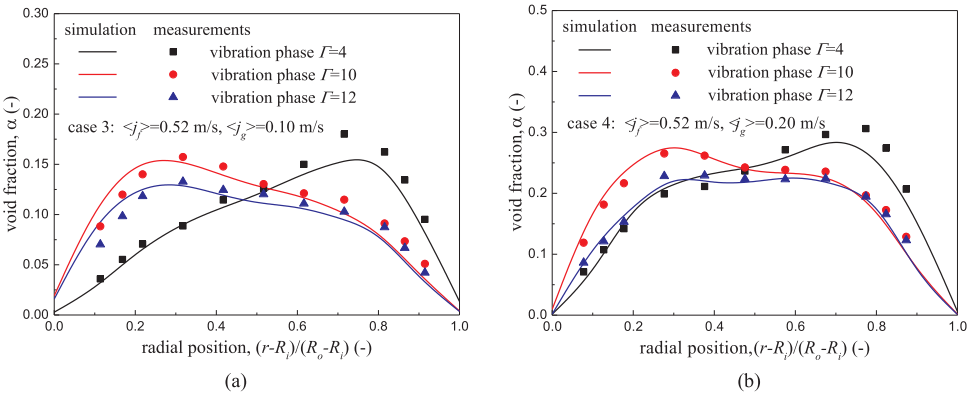

Fig. 10. Comparison of local void fraction distribution between simulation and experiments.

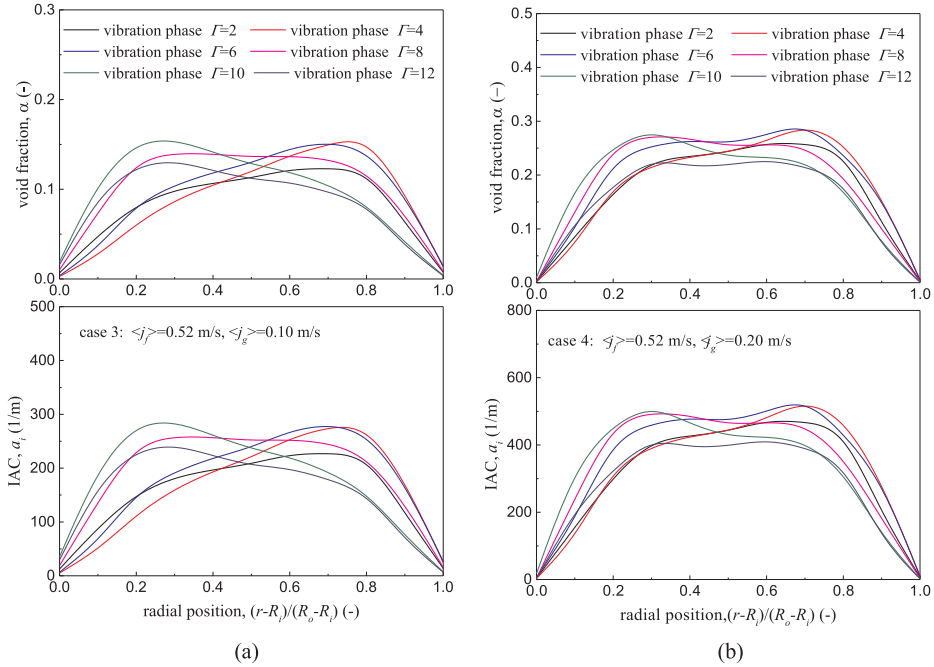

Fig. 11. Variations of void fraction and interfacial area concentration profiles in one vibration period.

that, in the cross section of the annulus, bubbles migrate along the vibration direction under the action of additional interfacial force. In the horizontal direction perpendicular to the vibration, the bubbles expelled from local positions are continuously replaced by the subsequent bubbles. As a result, the local interfacial parameters keep substantially constant during structure vibration. The simulation results

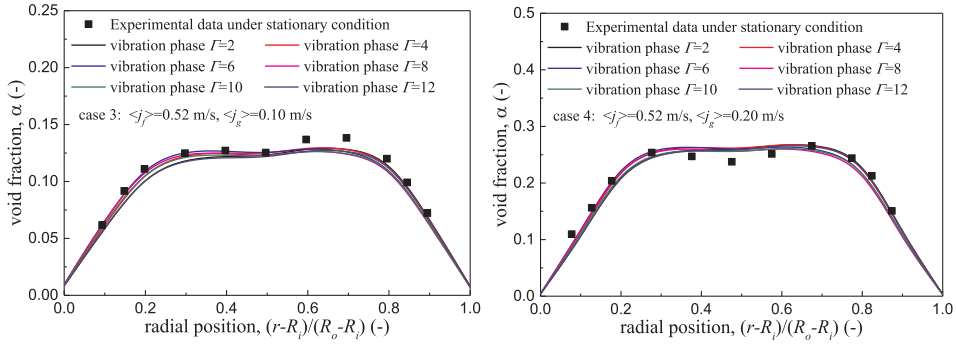

Fig. 12. Variations of void fraction profile along the radius perpendicular to the vibration direction.

are in good consistency with the parameters measured in the experiments under stationary condition. Thus, the current numerical modeling method provides a promising way for the prediction of phase distribution in bubbly flow regime under vibration condition.

5. Conclusions

In two-phase flow modeling, it is essential to take into account the interfacial forces including the drag force, lift force, wall lubrication force and turbulent dispersion force. In this study, the air–water two-phase flow distribution characteristics in a vertical upward annular channel were studied numerically. The predictive features of the up-to-date interfacial force models were firstly investigated. A total of four flow cases with different ranges of Re_b and Eo were used for model validation. Based on the results of this work, numerical simulations for bubbly flow under vibration condition were performed and the transient bubble transport phenomena induced by structure vibration were captured. The main conclusions obtained from the present work can be summarized as follows:

(1) The applicable performances of the presented interfacial force models vary with specific flow conditions in air–water two-phase flow. For bubbly flow in the vertical annular channel, model validation work was conducted and a set of Ishii-Zuber drag force model, Tomiyama lift force model, Frank wall force model and Burns turbulent dispersion force model was found to give the best agreement with the experimental results.
(2) The results of benchmark simulations indicated that the current modeling method can predict the distributions of local void fraction and interfacial area concentration with high accuracy for case 1, case 3 and case 4. But for case 2 with relatively high Re_b and Eo, poly-disperse nature may have become the main contributor to its flow characteristics and the poly-dispersed model considering bubble coalescence and breakup was suggested for such flow condition.
(3) A numerical modeling method was developed for bubbly flow under structure vibration condition. For the considered vibration condition, comparative analysis with the experimental results showed that the model can well depict the transient phase distributions of two-phase bubbly flow in the vibrating annular channel.
(4) The distributions of local interfacial parameters varied periodically along the direction of vibration. Specifically, an increase of about 32% in the peak void fraction was observed compared to that under stationary condition for case 3. But the local flow parameters remained substantially constant in the horizontal direction perpendicular to vibration.
(5) The current modeling method provides a promising tentative step towards an alternative way for analyzing the vibration-induced two-phase distribution instead of experimental method. But the modeling framework is based on two assumptions, which are (1) bubble coalescence and breakup can be neglected and (2) bubble diameter keeps constant along the flow direction. As a result, the simulation method is only limited to bubbly flow with relatively low void fraction and Eötvös number. Development of numerical modeling method for two-phase flow with bubble interactions is suggested in the future work.

CRediT authorship contribution statement

Xiu Xiao: Conceptualization, Methodology, Software, Writing - original draft, Funding acquisition. **Yu Guo:** Data curation, Writing - original draft. **Minyi Xu:** Investigation, Visualization. **Yulong Ji:** Software, Validation. **Qingzi Zhu:** Methodology, Writing - review & editing. **Mamoru Ishii:** Resources, Supervision.

Acknowledgements

Supports from the National Natural Science Foundation of China (Grant No. 51906029), China Postdoctoral Science Foundation funded project (Grant No. 2019M661084) and the Fundamental Research Funds for the Central Universities, China (Grants Nos. 3132019196 and 3132019331) are appreciated.

Declaration of interests

The authors declare that they have no known competing financial interests or personal relationships that could have appeared to influence the work reported in this paper.

References

Kataoka, I., Ishii, M., Serizawa, A., 1985. Local formulation and measurements of interfacial area concentration in two-phase flow. Int. J. Multiphase Flow 12 (4), 505–529.
Hibiki, T., Ishii, M., 1999. Experimental study on interfacial area transport in bubbly two-phase flows. Int. J. Heat Mass Transfer 42, 3019–3035.
Lucas, D., Krepper, E., Prasser, H.M., 2005. Development of co-current air-water flow in a vertical pipe. Int. J. Multiphase Flow 31, 1304–1328.
Yang, X., Schlegel, J.P., Liu, Y., Paranjape, S., Hibiki, T., Ishii, M., 2013. Experimental study of interfacial area transport in air-water two-phase flow in a scaled 88 BWR rod bundle. Int. J. Multiphase Flow 50, 16–32.
Tian, D., Yan, C., Sun, L., Tong, P., Liu, G., 2014. Comparison of local interfacial characteristics between vertical upward and downward two-phase flows using a four-sensor optical probe. Int. J. Heat Mass Transfer 77, 1183–1196.
Shen, X., Sun, H., Deng, B., Hibiki, T., Nakamura, H., 2017. Experimental study on interfacial area transport of two-phase bubbly flow in a vertical large diameter square duct. Int. J. Heat Fluid Flow 67, 168–184.
Skoczylas, A., Urbanski, A., 1992. Influence of vibrating element on heat transfer in a thin layer evaporator. Chemical Eng. J. 50 (3), 149–157.
Hibiki, T., Ishii, M., 1998. Effect of flow-induced vibration on local flow parameters of two-phase flow. Nucl. Eng. Des. 185, 113–125.
Mizuno, K., Kato, Y., Kaneko, A., Monji, H., Abe, Y., Yoshida, H., Takase, K., 2014. Experimental study on behavior of horizontal bubbly flow under structure vibration. Mech. Eng. J. 1.
Xiao, X., Zhu, Q., Chen, S.W., Zhang, Y., Jia, H., Ishii, M., 2017. Investigation on two-phase distribution in a vibrating annulus. Ann. Nucl. Energy 108, 67–78.

Chen, S.W., Hibiki, T., Ishii, M., Mori, M., Watanabe, F., 2017. Experimental investigation of horizontal forced-vibration effect on air-water two-phase flow. Int. J. Heat Fluid Flow 65, 33–46.
Ishii M., Hibiki T., 2010. Thermo-Fluid Dynamics of Two-Phase Flow. Springer, New York.
Wang, Q., Yao, W., 2016. Computation and validation of the interphase force models for bubbly flow. Int. J. Heat Mass Transfer 98, 799–813.
Lucas, D., Krepper, E., Prasser, H.M., 2004. Use of models for lift, wall and turbulent dispersion forces acting on bubbles for poly-disperse flows. Chem. Eng. Sci. 62, 4146–4157.
Rzehak, R., Krepper, E., Lifante, C., 2012. Comparative study of wall-force models for the simulation of bubbly flows. Nucl. Eng. Des. 253, 41–49.
Yamoah, S., Martinez-Cuenca, R., Monros, G., Chiva, S., Macian-Juan, R., 2015. Numerical investigation of models for drag, lift, wall lubrication and turbulent dispersion forces for the simulation of gas-liquid two-phase flow. Chem. Eng. Res. Des. 98, 17–35.
Chuang, T.J., Hibiki, T., 2017. Interfacial forces used in two-phase flow numerical simulation. Int. J Heat Mass Transfer 113, 741–754.
Menter, F.R., 1994. Two-equation eddy-viscosity turbulence models for engineering applications. AIAA J. 32, 1598–1605.
Wilcox D.C., 1998. Turbulence modelling for CFD. DCW industries, Inc., La Canada, California.
Sato, Y., Sekoguchi, K., 1975. Liquid velocity distribution in two-phase bubble flow. Int. J. Multiphase Flow 2 (1), 79–95.
Frank, Th., Zwart, P.J., Krepper, E., Prasser, H.M., Lucas, D., 2008. Validation of CFD models for mono- and polydisperse air-water two-phase flows in pipes. Nucl. Eng. Des. 238, 647–659.
Schiller, L., Naumann, A., 1935. A drag coefficient correlation. Vdi Zeitung 77 (318), 51.
Grace, J.R., Wairegi, T., Nguyen, T.H., 1976. Shapes and velocities of single drops and bubbles moving freely though immiscible liquids. Trans. Inst. Chem. Eng. 54, 167–173.
Ishii, M., Zuber, N., 1979. Drag coefficient and relative velocity in bubbly, droplet or particulate flows. AIChE J. 25, 843–855.
Launder, B.E., Spalding, D.B., 1974. The numerical computation of turbulent flows. Comput. Methods Appl. Mech. Eng. 3 (2), 269–289.
Legendre, D., Magnaudet, J., 1998. The lift force on a spherical bubble in a viscous linear shear flow. J. Fluid Mechanics 368, 81–126.
Tomiyama, A., 1998. Struggle with computational bubble dynamics. Multiphase Sci. Tech. 10, 369–405.
Antal, S.P., Lahey, R.T., Flaherty, J.E., 1991. Analysis of phase distribution in fully developed laminar bubbly two-phase flow. Int. J. Multiphase Flow 17 (5), 635–652.
Lopez de Bertodana M.A., 1992. Turbulent bubbly two-phase flow in a triangular duct (Ph.D. Thesis). Rensselaer Polytechnic Institute, Troy, New York.
Burns A.D., Frank T., Hamill I., Shi J.M., 2004. The Favre averaged drag model for turbulence dispersion in Eulerian multi-phase flows. In: Fifth International Conference on Multiphase Flow, ICMF-2004, Yokohama, Japan.
Chen S.W., 2012. Experimental Study of Seismic Vibration Effect on Two-Phase Flow (Ph. D. Thesis). Purdue University, West Lafayette, IN.
Sharma, S.L., Hibiki, T., Ishii, M., Schlegel Jr., J.P., Buchanan, J.R., Hogan, K.J., Guilbert, P.W., 2017. An interfacial shear term evaluation study for adiabatic dispersed air-water two-phase flow with the two-fluid model using CFD. Nucl. Eng. Des. 312, 389–398.
Sarı, S., Ergün, S., Barık, M., Kocar, C., Sökmen, C.N., 2009. Modeling of isothermal bubbly flow with ınterfacial area transport equation and bubble number density approach. Ann. Nucl. Energy 36, 222–232.